

Novel electronic state of honeycomb iridate Cu_2IrO_3 at high pressure

G. Fabbris,^{1,*} E. H. T. Poldi,^{1,2} S. Sinha,³ J. Lim,³ T. Elmslie,³ J. H. Kim,¹ A. Said,¹ M. Upton,¹ M. Abramchuk,⁴ F. Bahrami,⁴ C. Kenney-Benson,⁵ C. Park,⁵ G. Shen,⁵ Y. K. Vohra,⁶ R. J. Hemley,^{2,7} J. J. Hamlin,³ F. Tafti,⁴ and D. Haskel¹

¹*Advanced Photon Source, Argonne National Laboratory, Lemont, Illinois 60439, USA*

²*Department of Physics, University of Illinois at Chicago, Chicago, Illinois 60607, USA*

³*Department of Physics, University of Florida, Gainesville, Florida 32611, USA*

⁴*Physics Department, Boston College, Chestnut Hill, Massachusetts 02467, USA*

⁵*HPCAT, Advanced Photon Source, Argonne National Laboratory, Lemont, Illinois 60439, USA*

⁶*Department of Physics, University of Alabama at Birmingham, Birmingham, Alabama 35294, USA*

⁷*Departments of Chemistry, and Earth and Environmental Sciences, University of Illinois Chicago, Chicago, Illinois 60607, USA*

(Dated: October 7, 2024)

Cu_2IrO_3 has attracted recent interest due to its proximity to the Kitaev quantum spin liquid state and the complex structural response observed at high pressures. We use x-ray spectroscopy and scattering as well as electrical transport techniques to unveil the electronic structure of Cu_2IrO_3 at ambient and high pressures. Despite featuring a $\text{Ir}^{4+} J_{\text{eff}} = 1/2$ state at ambient pressure, Ir L_3 edge resonant inelastic x-ray scattering reveals broadened electronic excitations that point to the importance of Ir 5d-Cu 3d interaction. High pressure first drives an Ir-Ir dimer state with collapsed $\langle \mathbf{L} \cdot \mathbf{S} \rangle$ and $\langle L_z \rangle / \langle S_z \rangle$, signaling the formation of 5d molecular orbitals. A novel $\text{Cu} \rightarrow \text{Ir}$ charge transfer is observed at the onset of phase 5 above 30 GPa at low temperatures, leading to an approximate Ir^{3+} and $\text{Cu}^{1.5+}$ valence, with persistent insulating electrical transport seemingly driven by charge segregation of Cu 1+/2+ ions into distinct sites. Concomitant x-ray spectroscopy and scattering measurements through different thermodynamic paths demonstrate a strong electron-lattice coupling, with $J_{\text{eff}} = 1/2$ and $\text{Ir}^{3+}/\text{Cu}^{1.5+}$ electronic states occurring only in phases 1 and 5, respectively. Remarkably, the charge-transferred state can only be reached if Cu_2IrO_3 is pressurized at low temperature, suggesting that phonons play an important role in the stability of this phase. These results point to the choice of thermodynamic path across interplanar collapse transition as a key route to access novel states in intercalated iridates.

The realization that strong spin-orbit coupling can drive electronic correlation and emergent phenomena has revolutionized research on heavy transition metals materials [1–3]. Particular attention has been devoted to the emergence of $J_{\text{eff}} = 1/2$ orbitals in Ir^{4+} and its consequences [4, 5], with recent focus centered on the theoretically predicted Kitaev quantum spin liquid (QSL) state due to its potential use in topologically protected quantum computing [6]. Fundamentally, the Kitaev QSL is an analytically solvable Hamiltonian that relies on a combination of a 2D honeycomb structural lattice and bond-directional exchange interaction, with the spin-orbit-driven $J_{\text{eff}} = 1/2$ state of honeycomb iridates being strong candidate to realize these conditions [5]. However, stabilizing this state has proven to be difficult since, in real materials, other magnetic interactions are not fully quenched and compete with the Kitaev exchange, usually leading to magnetic order as in Li_2IrO_3 and Na_2IrO_3 [7–11]. The recent development of intercalated honeycomb iridates, namely Cu_2IrO_3 [12], $\text{Ag}_3\text{LiIr}_2\text{O}_6$ [13], and $\text{H}_3\text{LiIr}_2\text{O}_6$ [14], has re-ignited the field since magnetic order is suppressed in these materials. However, the intercalation process drives structural disorder and can disrupt the Ir $J_{\text{eff}} = 1/2$ orbital [15–17], raising questions on whether the Kitaev QSL has indeed been stabilized.

Cu_2IrO_3 is distinct to other intercalated iridates by

the presence of Cu ions both between and within the Ir honeycomb layer [Figs. 1(a,b)] [12, 18]. This leads to the unusual octahedrally coordinated Cu^{1+} ions in plane. There is evidence for the presence of magnetic Cu^{2+} ($\sim 10\%$), which is argued to be nucleated in $\text{Cu}^{2+}/\text{Ir}^{3+}$ domains [15]. The apparent proximity between these charge states raises the potential for structural control of the electronic and/or magnetic properties. Indeed, Cu_2IrO_3 displays a very rich high pressure structural phase diagram [19–21], featuring distinct sets of phase transitions at room and low temperatures [Figs. 1(c,d)] [19]. Low pressures ($\sim 6 - 7.5$ GPa) drive Ir-Ir dimerization (phase 2) [19–21], similar to reports on Li_2IrO_3 polymorphs [22–25] and $\text{Ag}_3\text{LiIr}_2\text{O}_6$ [26]. Higher pressures lead to the collapse of the interplanar distance and a distinct structural temperature dependence, with phase 3 appearing around 15 GPa at room temperature (RT), and phases 4 and 5 around 18 GPa and 30 GPa at low temperature, respectively [19]. While a substantial drop in resistance is observed at onset of phase 3 [20, 21], there is little information on if and/or how the electronic structure is coupled to these phase transitions.

In this work, we investigate the relationship between the crystal and electronic structure in Cu_2IrO_3 using x-ray absorption near edge structure (XANES), x-ray magnetic circular dichroism (XMCD), resonant inelastic x-

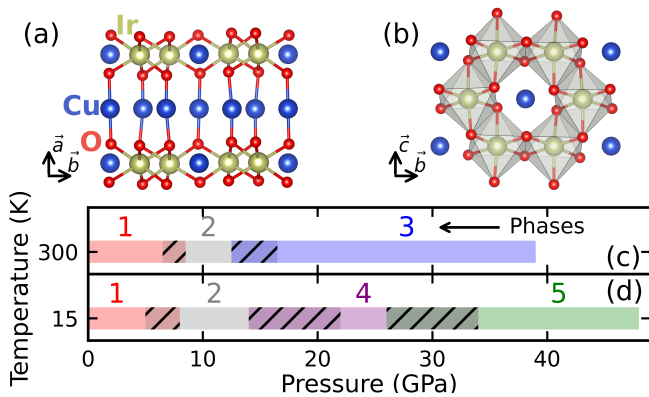


FIG. 1. (a)&(b) Crystal structure at ambient pressure featuring Ir honeycomb layers and interplanar O-Cu-O dumbbells. (c)&(d) High pressure phase diagram of Cu_2IrO_3 at room and low temperature [19], respectively, as determined through isotherm measurements. The dashed areas are regions of coexistence of two phases.

ray scattering (RIXS), x-ray powder diffraction, and electrical transport measurements as a function of pressure and temperature. The data reveal that the Ir-Ir dimerization in phase 2 suppresses the localized $J_{\text{eff}} = 1/2$, which is phenomenologically similar to Li_2IrO_3 polymorphs [22, 23, 25, 27]. Further compression at low temperature drives a $\text{Cu} \rightarrow \text{Ir}$ electron transfer at the onset of phase 5. Despite the Cu mixed valency, Cu_2IrO_3 remains an insulator in phase 5, which appears to be due to charge segregation into $\text{Cu}^{1+}/\text{Cu}^{2+}$ sites. No charge transfer occurs at similar pressure at RT (phase 3). Remarkably, no electronic or structural phase transition is observed upon cooling from phase 3 (RT to 15 K) or warming from phase 5 (15 K to RT). This demonstrates a strong electron-lattice coupling as the charge transfer is intrinsically connected to the phase 5 structure. It also points to an intricate phase stability landscape in Cu_2IrO_3 , with distinct phenomenology driven by the specific thermodynamic path.

We start by addressing the electronic structure of Cu_2IrO_3 in phase 1 at ambient pressure. Intercalated honeycomb iridates were conceived to reduce the exchange interaction between the honeycomb layers, while preserving the well defined $J_{\text{eff}} = 1/2$ character seen in Na_2IrO_3 and Li_2IrO_3 , leading to a more 2D structural motif that better mimics the Kitaev model [6]. To explore the detailed electronic structure of Cu_2IrO_3 XANES and XMCD were measured at the 4-ID-D and RIXS at the 27-ID beamlines of the Advanced Photon Source (APS), Argonne National Laboratory (ANL). All measurements were performed in powdered samples that were grown as described in ref. [12], and XMCD was collected using a magnetic field of 4 T. Experimental details are described in the Supplemental Material [28]. At ambient pressure, Cu_2IrO_3 displays the typical Ir^{4+} XANES and XMCD

spectra [Fig. 2(a-d)], featuring large L_3/L_2 intensity ratio. Sum rules analysis reveals $\langle \mathbf{L} \cdot \mathbf{S} \rangle = 2.64(3) \hbar^2$ and $\langle L_z \rangle / \langle S_z \rangle = 2.4(1)$ [29–31], which is consistent with other honeycomb iridates [17, 22, 25, 32] and, more generally, with $J_{\text{eff}} = 1/2$ Ir oxides [32–35].

RIXS measurements, however, point to a more complex picture, with meaningful differences in the orbital excitations among the honeycomb iridates. Na_2IrO_3 and $\alpha - \text{Li}_2\text{IrO}_3$ feature an exciton peak at $\sim 420 - 450$ meV, and a pair of trigonal crystal field split $J_{\text{eff}} = 3/2$ peaks at about 720 – 830 meV [36]. A markedly different excitation spectra is observed in $\text{Ag}_3\text{LiIr}_2\text{O}_6$, with theoretical modeling pointing to a substantially larger Ir-O hybridization, which is argued to enhance magnetic frustration [17]. In Cu_2IrO_3 , a low energy peak is clearly observed at the Ir L_3 , but not at the L_2 , demonstrating the $J_{\text{eff}} = 1/2$ ground state [Fig. 2(g)]. However, while the spectra appears to be composed of three peaks, these are largely broadened compared to other honeycomb iridates [17, 25, 36, 37]. Since measurements were done in powdered Cu_2IrO_3 , this suggests more dispersive J_{eff} excitations, which points to an increased delocalization of the 5d orbitals. Finally, compared to Cu_2IrO_3 and $\text{Ag}_3\text{LiIr}_2\text{O}_6$, $\text{H}_3\text{LiIr}_2\text{O}_6$ features electronic excitations that much closer resemble those of $\alpha - \text{Li}_2\text{IrO}_3$ [17, 36, 37], indicating that the use of a d-electron-based intercalation ion plays a key role in disrupting the Ir 5d orbital.

We now explore the relationship between the high pressure structural phase diagram and the electronic structure of Cu_2IrO_3 . Pressure drives the onset of phase 2 at both room (6 ± 1.5 GPa) and low (7.5 ± 1 GPa) temperatures [Figs. 1(c,d)], featuring Ir-Ir structural dimers [19]. The emergence of phase 2 is closely correlated with a disruption of the $J_{\text{eff}} = 1/2$ state, as seen by the reduction of $\langle \mathbf{L} \cdot \mathbf{S} \rangle$ and $\langle L_z \rangle / \langle S_z \rangle$ [Fig. 2(e,f)], as well as the suppression of the low energy excitation ($J_{\text{eff}} = 3/2$, < 1 eV) [Fig. 2(g)]. These results are similar to those observed at the dimerization of $\alpha -$ and $\beta - \text{Li}_2\text{IrO}_3$ [22–25, 27, 38]. However, contrary to Li_2IrO_3 [25, 27], new low energy RIXS excitations are not seen in Cu_2IrO_3 , instead an increase in the incoherent continuum is observed [Fig. 2(g)]. Quasimolecular orbitals are likely also stabilized in Cu_2IrO_3 , but the influence of hybridization with Cu 3d orbitals masks their low energy excitations. Notably, however, while the exact nature of the quasimolecular orbital cannot be determined, there is strong evidence for the persistent importance of spin orbit coupling (SOC). Both $\langle \mathbf{L} \cdot \mathbf{S} \rangle$ and $\langle L_z \rangle / \langle S_z \rangle$ remain sizeable. But more strikingly, the RIXS excitation near 2.2 eV, which at ambient pressure is related to the SOC split t_{2g} band [36], not only persists at the Ir L_3 edge, but remains absent at the Ir L_2 [Fig. 2(g)]. These results are consistent with a picture that includes both large hopping between the dimerized Ir and large SOC, as described for other iridates [38–41]. Finally, an increase in resistance is ob-

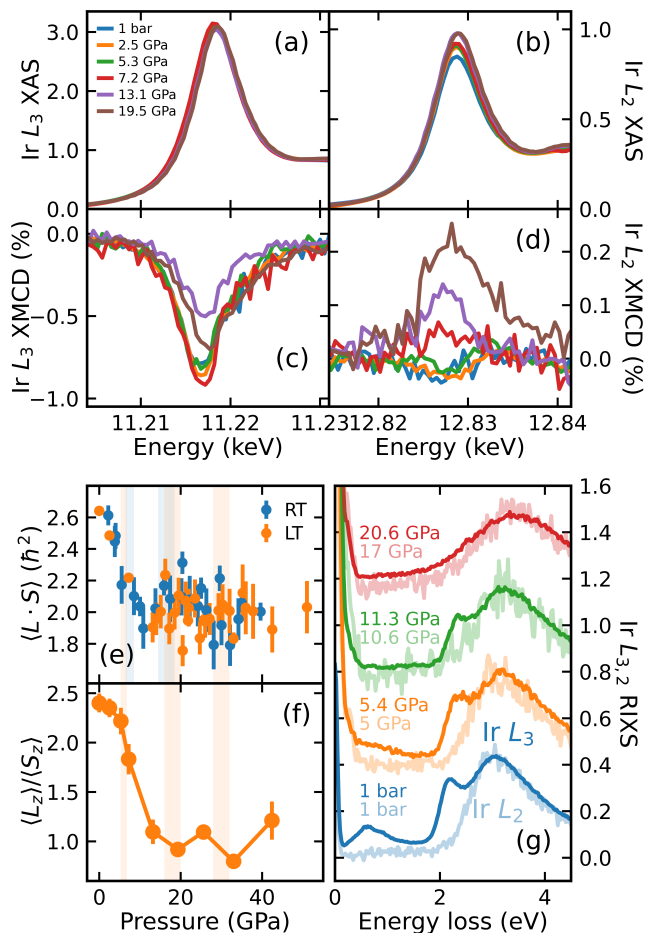


FIG. 2. Electronic properties of Cu_2IrO_3 across the dimerization transition. (a)-(d) Pressure dependence of the Ir $L_{3,2}$ XANES and XMCD spectra at low temperature. Sum rules analysis of the XANES and XMCD yields the (e) average spin-orbit coupling and (f) orbital to spin moment ratio. (g) RIXS pressure dependence at the Ir L_3 (11.215 keV incident energy) and L_2 (12.821 keV) at room temperature.

served at the dimerization onset at RT [Fig. 3(j)], consistent with a previous report [20], and in agreement with a larger band gap obtained from density functional theory (DFT) calculations [19].

While the onset of phase 2 primarily affects the Ir $5d$ state, the Cu orbitals become active at higher pressures. Curiously, the large reduction in interplanar distance (d) at the onset of phase 3 ($\Delta d/d \approx 8\%$ [19, 28]) is not reflected in the Ir $L_{3,2}$ XANES, with no distinct changes to $\langle \mathbf{L} \cdot \mathbf{S} \rangle$ or $5d$ occupation [Figs. 2(e) and 3(k)]. However, the RIXS excitation near 2.2 eV disappears in phase 3 [Fig. 2(g)], and an intense continuum of excitation develops, extending to zero energy loss. A similar increase in the incoherent background is seen at the Ir L_2 RIXS [Fig. 2(g)]. These results suggest that the electronic structure of phase 3 features strongly hybridized Ir $5d$ -Cu $3d$ orbitals that destroy the quasimolecular orbitals

of phase 2, and is consistent with the substantial drop in resistance [Fig. 3(j)]. The electrical resistance temperature dependence points to a possible metallicity near the onset of phase 3, with increasing semiconducting behavior at higher pressures [20, 28], but, as shown below, phase 3 is sensitive to the thermodynamic path, complicating the interpretation of these results. The nature of these orbitals is potentially interesting as $\langle \mathbf{L} \cdot \mathbf{S} \rangle$ remains sizeable, suggesting that, despite the collapse of the J_{eff} state and quasimolecular orbitals, SOC still plays an important role. No energy shift is observed in the Cu K edge spectra, indicating that its modification is likely a structural response due to strongly modified interplanar O-Cu-O dumbbells, likely without an increase in the Cu coordination.

At low temperature, the onset of phase 5 is marked by a reduction in the Ir $L_{3,2}$ white line area and shift in the Cu K edge energy (Fig. 3). Assuming that 80% of Ir are $4+$ at low pressures ($\langle n_h \rangle = 4.8$, where $\langle n_h \rangle$ is the number of $5d$ holes) [15], the reduction in the white line area implies $\langle n_h \rangle \sim 3.9$ above 30 GPa [Fig. 3(k)], i.e. an approximate Ir^{3+} . The Cu valence can be extracted by the position of the absorption edge, which is defined as the maximum of the XANES first derivative. While the multi-featured Cu K edge of Cu_2IrO_3 largely complicates a quantitative analysis, a clear change in the first derivative is seen at the onset of phase 5 [Fig. 3(i)], leading to a discontinuous jump in position of the absorption edge [Fig. 3(l)]. Notably, the Cu K edge taken in phase 3 is very distinct, and features a lower energy edge [Fig. 3(i)]. The sharpness of this jump is artificial as the maximum moves from the first to the second peak in the XANES derivative [Fig. 3(i)]. Nevertheless, the increase in energy implies that Cu lost electrons, thus demonstrating a novel Cu \rightarrow Ir electron transfer in Cu_2IrO_3 that occurs only in phase 5. The substantial difference in the electronic structure of phases 3 and 5 indicates that these phases likely feature distinct Cu environments, despite similar collapsed interplanar distances and stability pressure range.

The Ir^{3+} state implies that the nominal Cu valence is $1.5+$. Metallic electronic transport would be expected if this partial valence was only due to the delocalization of the Cu $3d$ bands. However, while a large drop in resistance is observed at pressures near the phase 5 onset, its temperature dependence points to a persistent electronic gap [inset of Fig. 3(j)]. Although the maximum of the Cu K edge derivative shifts in phase 5, a sizeable spectral weight is observed at the Cu 1^{5+} energy [Fig. 3(i)], indicating that the average $\text{Cu}^{1.5+}$ is formed by a mixture of $2+$ and $1+$ ions. The Ir^{3+} $5d^6$ orbital features fully occupied t_{2g} states, with a large octahedral crystal field [~ 3.5 eV, Fig. 2(g)]. Therefore, while increased Cu/Ir hybridization leads to a lower resistance in phase 5, the Ir^{3+} configuration combined with the Cu charge segregation results in the insulating behavior. Interest-

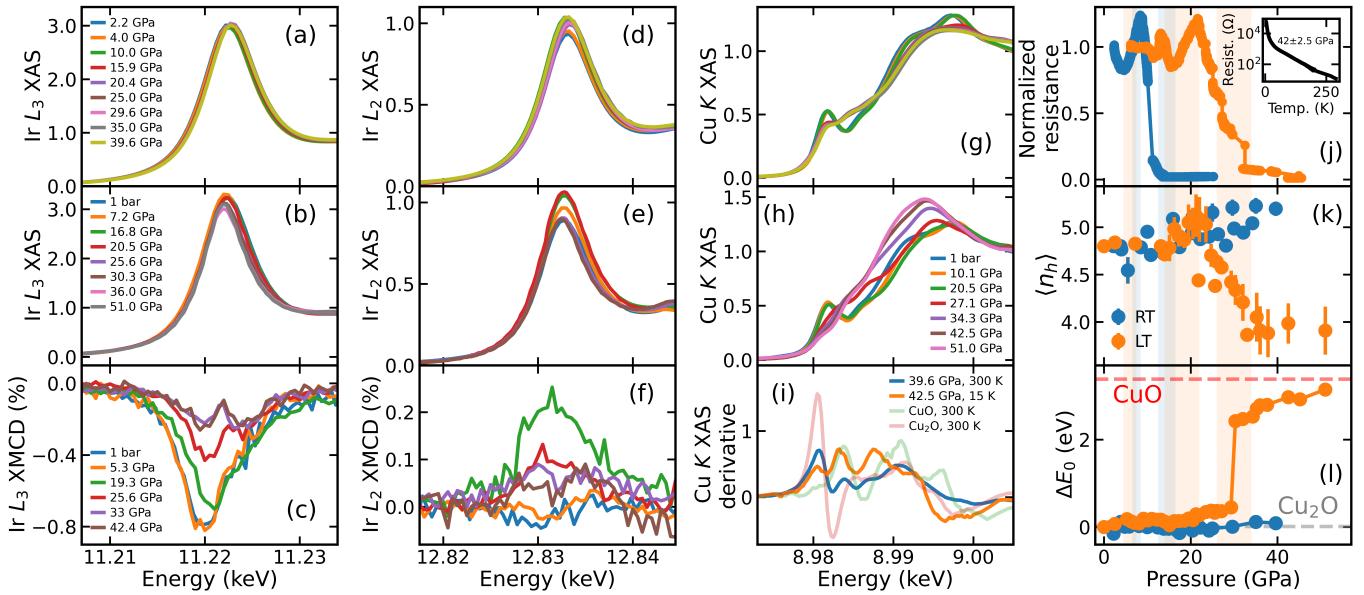


FIG. 3. Electronic properties of Cu_2IrO_3 across phases 3, 4 and 5. Panels (a-c) and (d-f) display the pressure dependence of the room and low temperature XANES as well as low temperature XMCD taken at the Ir L_3 and L_2 edges, respectively. (g)&(h) Cu K edge XANES at room and low temperature, respectively. Panels (d)&(g) follow the same legend as (a). (i) Comparison between the Cu K edge XANES derivative of Cu references (Cu_2^{1+}O and Cu^{2+}O) and Cu_2IrO_3 at room and low temperature taken at approximately the same pressure (corresponding to phases 3 and 5). (j) Resistance pressure dependence at room and low temperatures. The resistance was normalized to its value at ambient pressure (42 Ω and 584 Ω at room and low temperatures, respectively). Inset: resistance temperature dependence upon warming at 42 ± 2.5 GPa showing that phase 5 remains insulating. (k)&(l) Number of $5d$ holes ($\langle n_h \rangle$) and Cu K edge shift at room and low temperatures extracted from XANES data. An electron transfer from Cu to Ir occurs only at the onset of phase 5. Vertical shaded areas in panels (j-l) correspond to the structural phase transition regions at RT (blue) and low temperature (orange) [19].

ingly, this scenario is consistent with DFT calculations, despite phase 5 being different from the predicted crystal structure [19]. Finally, the localized Cu^{2+} ions in phase 5 could drive magnetism. In fact, the small anti-ferromagnetic response of Cu_2IrO_3 at ambient pressure is attributed to the $\text{Cu}^{2+}/\text{Ir}^{3+}$ minority domains [12, 15]. However, no signal XMCD signal was observed at the Cu K edge [28]. While this suggests that Cu is not ferromagnetically ordered, it does not discard a possible antiferromagnetic state.

Copper delafossites feature a similar crystal structure pressure dependence to Cu_2IrO_3 , albeit with a triangular lattice [42]. Interestingly, while a pressure-driven interplanar collapse appears to be a general behavior in these compounds [43–47], only CuFeO_2 is known to feature a similar valence transition [43, 44]. While there is not an established explanation for this behavior, it suggests that the valence transition depends on the relative chemical potential of the related ions. This raises questions on the high pressure behavior of other intercalated iridates. Recently, an unidentified structural transition was reported in $\text{Ag}_3\text{LiIr}_2\text{O}_6$ around 12–16.1 GPa at RT, which occurs concomitantly to a change in sign of the magnetoresistance [26]. This phenomenology is similar to that seen in Cu_2IrO_3 [20], and points to a potential valence instabil-

ity.

The dramatic temperature dependence of the electronic structure of Cu_2IrO_3 led us to explore its thermodynamics through concomitant powder x-ray diffraction and Ir $L_{3,2}$ as well as Cu K edge XANES collected at the HPCAT 16-BM-D beamline at the APS, ANL [28]. Two temperature/pressure paths were taken: 1) pressure was applied at 300 K up to 38 GPa, followed by a nearly isobaric cool down to 14 K (pressure was maintained between 38 and 41 GPa), and low temperature decompression; 2) sample was cooled down to 14 K keeping the pressure below 5 GPa, then pressurized to 38.7 GPa at low temperature, followed by a nearly isobaric warm up to 300 K (pressure was kept between 38.7 and 43 GPa), and 300 K decompression. These different paths drive distinct sets of phase transitions. The compression in path 1) reproduces the phase transitions seen in our previous work [19], stabilizing phase 3 beyond ~ 18 GPa with collapsed interplanar distance [Fig. 4(a)]. High pressure cool down preserves phase 3, which remains stable upon low temperature pressure release to at least 22.5 GPa. Path 2) again leads to the same set of reported low-temperature phases [Fig. 4(b)] [19]. Remarkably, phase 5 is also preserved upon warming up to 300 K. Pressure release at 300 K leads to a phase 5 \rightarrow 3 transition at 27 ± 3 GPa,

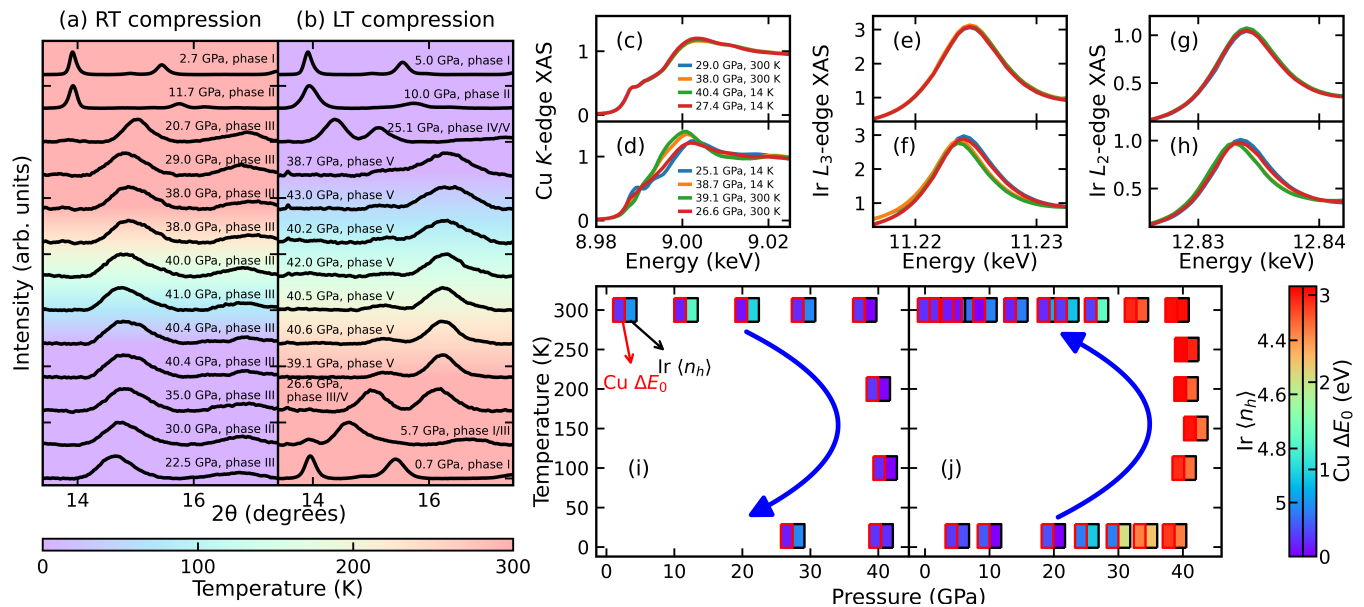


FIG. 4. Structural and electronic properties of Cu_2IrO_3 through two distinct thermodynamical paths. (a), (c), (e) and (g) display x-ray diffraction as well as Cu K and Ir $L_{3,2}$ edge XANES measured while pressurizing at RT and depressurizing at 15 K, respectively, while (b), (d), (f), and (h) display the same measurements taken via the reverse path. (i)&(j) Number of $5d$ holes ($\langle n_h \rangle$) and the shift in Cu K edge energy are shown for each path.

but no signs of phase 4. The dimerized phase 2 is also not detected on pressure release. The remarkable phase diagram of Cu_2IrO_3 is closely followed by the electronic structure [Fig. 4(c-j)]. The Cu \rightarrow Ir electron transfer occurs only within phase 5, with the reversal to the approximate $\text{Ir}^{4+}/\text{Cu}^{1+}$ configuration at the phase 5 \rightarrow 3 transition, and the $J_{\text{eff}} = 1/2$ state features only in phase 1, again including on pressure release through path 2). These results highlight a strong electron-lattice coupling in Cu_2IrO_3 .

The RT phase diagram of Cu_2IrO_3 is not settled in the literature [19–21] (there is only one report on the low temperature structures [19]). While there is an overall agreement on the presence of a dimerized Ir-Ir and interplanar collapsed structures (phases 2 and 3), different critical and coexistence pressures have been reported. A key difference amongst these studies is the use of different pressure media, which likely leads to different hydrostaticity. The absence of phase 2 upon decompression from phase 5 further points to the importance of the non-hydrostatic shear in the phase stability of Cu_2IrO_3 , since decompression leads to large pressure gradients. The Cu_2IrO_3 growth method may also be relevant to the high pressure phase stability, as recent developments have led to less structural disorder [48]. Additionally, our results suggest that previous transport measurements did not probe the properties of phases 4 or 5, as pressure was applied at RT [20, 21]. Although our data [Fig. 3(j)] and theoretical calculations indicate that Cu_2IrO_3 is an insulator in phase 5, due to the distinct pressure media used in these measurements, concomitant electrical transport

and x-ray diffraction measurements are needed to verify this result.

The process behind phases 3, 4, 5 stability remains an important open topic given their distinct electronic properties. The absence of a phase 3 \rightarrow 5 (5 \rightarrow 3) transition upon cooling (warming) at high pressure prevents determining whether one of these is the ground state. The onset of phase 4 at a similar pressure to phase 3 indicates that its presence is important in stabilizing phase 5. Both of these phases feature a collapsed interplanar distance, which is likely associated with modifications in the O-Cu-O dumbbells (note that this distance is nearly pressure-independent in phases 1 and 2) [19, 28]. Such interplanar dumbbells typically feature strong low energy phonons [47, 49]. Therefore, it is likely that the stability of these phases is closely tied to the vibrational amplitude of the dumbbell phonons. This scenario implies that a similar phenomenology will occur in $\text{H}_3\text{LiIr}_2\text{O}_6$ and $\text{Ag}_3\text{LiIr}_2\text{O}_6$. Alternatively, low temperature might stifle the nucleation and growth of phase 3, stabilizing instead phase 4. It would be interesting to probe whether the speed of compression affects this transition [50] (in this work, we typically pressurized at ~ 50 GPa/h, stopping at each pressure point for about 10 – 30 min). Further exploration of the Cu_2IrO_3 thermodynamic landscape is needed, not only to clarify the role and stability of phase 4, but also to search for novel phenomena.

In conclusion, our work explores the pressure dependence of the electronic properties of Cu_2IrO_3 . At ambient pressure, an enhanced delocalization of $5d$ $J_{\text{eff}} = 1/2$ orbitals is observed, likely driven by hybridization with

the in-plane Cu $3d$ orbitals. High pressure data unveils a remarkable electronic phase diagram. The dimerized Ir-Ir bonds of phase 2 lead to a collapse of the $J_{\text{eff}} = 1/2$ state, likely stabilizing molecular orbitals with persistent J_{eff} character. Higher pressures lead to the collapse of the interplanar distances, and to large changes in the electronic structure. While the RT phase 3 feature dominant $\text{Ir}^{4+}/\text{Cu}^{1+}$ ions, the low temperature phase 5 stabilizes $\text{Ir}^{3+}/\text{Cu}^{1.5+}$. The insulating behavior of phase 5 appears to originate in a charge segregation of Cu $1+$ and $2+$, raising the prospect of antiferromagnetic order. A remarkable temperature dependence is seen at high pressures with phase 5 only being stabilized upon cold compression, but remaining stable upon warming to 300 K. The richness of the Cu_2IrO_3 phase diagram motivates further work. Additionally, it highlights the importance of investigating other intercalated iridates, and the role of the thermodynamic path in driving novel phenomena.

We thank Richard Ferry for the support during experiments at HPCAT. This research used resources of the APS, a U.S. Department of Energy (DOE) Office of Science user facility at ANL and is based on research supported by the U.S. DOE Office of Science-Basic Energy Sciences, under Contract No. DE-AC02-06CH11357. Portions of this work were performed at HPCAT (Sector 16), APS, ANL. HPCAT operations are supported by DOE-NNSA's Office of Experimental Sciences. Helium and neon pressure media were loaded at GeoSoilEnviroCARS (The University of Chicago, Sector 13), APS, ANL. GeoSoilEnviroCARS was supported by the National Science Foundation – Earth Sciences (EAR – 1634415). The work at Boston College was funded by the U.S. Department of Energy, Office of Basic Energy Sciences, Division of Physical Behavior of Materials under award number DE-SC0023124. Work at the at the University of Florida was supported by NSF DMR-2118718. The UIC effort was supported by NSF grants DMR-2119308 and DMR-2118020, and by the DOE-NNSA cooperative agreement DE-NA-0003975 (Chicago/DOE Alliance Center, CDAC).

* gfabbris@anl.gov

- [1] W. Witczak-Krempa, C. Gang, K. Y. Baek, and B. Leon, Correlated quantum phenomena in the strong spin-orbit regime, *Annual Review of Condensed Matter Physics* **5**, 57 (2014).
- [2] J. G. Rau, E. K.-H. Lee, and H.-Y. Kee, Spin-orbit physics giving rise to novel phases in correlated systems: Iridates and related materials, *Annual Review of Condensed Matter Physics* **7**, 195 (2016).
- [3] G. Cao and P. Schlottmann, The challenge of spin-orbital ground states in iridates: a key issues review, *Reports on Progress in Physics* **81**, 042502 (2018).
- [4] B. J. Kim, H. Ohsumi, T. Komesu, S. Sakai, T. Morita, H. Takagi, and T. Arima, Phase-Sensitive Observation of a Spin-Orbital Mott State in Sr_2IrO_4 , *Science* **323**, 1329 (2009).
- [5] G. Jackeli and G. Khaliullin, Mott Insulators in the Strong Spin-Orbit Coupling Limit: From Heisenberg to a Quantum Compass and Kitaev Models, *Physical Review Letters* **102**, 017205 (2009).
- [6] A. Kitaev, Anyons in an exactly solved model and beyond, *Annals of Physics* **321**, 2 (2006).
- [7] X. Liu, T. Berlijn, W. G. Yin, W. Ku, A. Tsvelik, Y.-J. Kim, H. Gretarsson, Y. Singh, P. Gegenwart, and J. P. Hill, Long-range magnetic ordering in Na_2IrO_3 , *Physical Review B* **83**, 220403(R) (2011).
- [8] F. Ye, S. Chi, H. Cao, B. C. Chakoumakos, J. A. Fernandez-Baca, R. Custelcean, T. F. Qi, O. B. Korneta, and G. Cao, Direct evidence of a zigzag spin-chain structure in the honeycomb lattice: A neutron and x-ray diffraction investigation of single-crystal Na_2IrO_3 , *Physical Review B* **85**, 180403(R) (2012).
- [9] A. Biffin, R. D. Johnson, S. Choi, F. Freund, S. Manni, A. Bombardi, P. Manuel, P. Gegenwart, and R. Coldea, Unconventional magnetic order on the hyperhoneycomb Kitaev lattice in $\beta\text{-Li}_2\text{IrO}_3$: Full solution via magnetic resonant x-ray diffraction, *Physical Review B* **90**, 205116 (2014).
- [10] S. Hwan Chun, J.-W. Kim, J. Kim, H. Zheng, C. C. Stoumpos, C. D. Malliakas, J. F. Mitchell, K. Mehlawat, Y. Singh, Y. Choi, T. Gog, A. Al-Zein, M. M. Sala, M. Krisch, J. Chaloupka, G. Jackeli, G. Khaliullin, and B. J. Kim, Direct evidence for dominant bond-directional interactions in a honeycomb lattice iridate Na_2IrO_3 , *Nature Physics* **11**, 462 (2015).
- [11] S. C. Williams, R. D. Johnson, F. Freund, S. Choi, A. Jesche, I. Kimchi, S. Manni, A. Bombardi, P. Manuel, P. Gegenwart, and R. Coldea, Incommensurate counter-rotating magnetic order stabilized by Kitaev interactions in the layered honeycomb $\alpha\text{-Li}_2\text{IrO}_3$, *Physical Review B* **93**, 195158 (2016).
- [12] M. Abramchuk, C. Ozsoy-Keskinbora, J. W. Krizan, K. R. Metz, D. C. Bell, and F. Tafti, Cu_2IrO_3 : A New Magnetically Frustrated Honeycomb Iridate, *Journal of the American Chemical Society* **139**, 15371 (2017).
- [13] F. Bahrami, W. Lafargue-Dit-Hauret, O. I. Lebedev, R. Movshovich, H.-Y. Yang, D. Broido, X. Rocquefelte, and F. Tafti, Thermodynamic evidence of proximity to a Kitaev spin liquid in $\text{Ag}_3\text{LiIr}_2\text{O}_6$, *Physical Review Letters* **123**, 237203 (2019).
- [14] K. Kitagawa, T. Takayama, Y. Matsumoto, A. Kato, R. Takano, Y. Kishimoto, S. Bette, R. Dinnebier, G. Jackeli, and H. Takagi, A spin-orbital-entangled quantum liquid on a honeycomb lattice, *Nature* **554**, 341 (2018).
- [15] E. M. Kenney, C. U. Segre, W. Lafargue-Dit-Hauret, O. I. Lebedev, M. Abramchuk, A. Berlie, S. P. Cottrell, G. Simutis, F. Bahrami, N. E. Mordvinova, G. Fabbris, J. L. McChesney, D. Haskel, X. Rocquefelte, M. J. Graf, and F. Tafti, Coexistence of static and dynamic magnetism in the Kitaev spin liquid material Cu_2IrO_3 , *Physical Review B* **100**, 094418 (2019).
- [16] J. Knolle, R. Moessner, and N. B. Perkins, Bond-disordered spin liquid and the honeycomb iridate $\text{H}_3\text{LiIr}_2\text{O}_6$: Abundant low-energy density of states from random majorana hopping, *Physical Review Letters* **122**, 047202 (2019).
- [17] A. de la Torre, B. Zager, F. Bahrami, M. DiScala, J. R.

- Chamorro, M. H. Upton, G. Fabbris, D. Haskel, D. Casa, T. M. McQueen, F. Tafti, and K. W. Plumb, Enhanced hybridization in the electronic ground state of the intercalated honeycomb iridate $\text{Ag}_3\text{LiIr}_2\text{O}_6$, *Physical Review B* **104**, L100416 (2021).
- [18] F. Bahrami, M. Abramchuk, O. Lebedev, and F. Tafti, Metastable Kitaev magnets, *Molecules* **27**, 871 (2022).
- [19] G. Fabbris, A. Thorn, W. Bi, M. Abramchuk, F. Bahrami, J. H. Kim, T. Shinmei, T. Irifune, F. Tafti, A. N. Kolmogorov, and D. Haskel, Complex pressure-temperature structural phase diagram of the honeycomb iridate Cu_2IrO_3 , *Physical Review B* **104**, 014102 (2021).
- [20] C. Jin, Y. Wang, M. Jin, Z. Jiang, D. Jiang, J. Li, Y. Nakamoto, K. Shimizu, and J. Zhu, Insulator-metal transition and crossover from negative to positive magnetoresistance in Cu_2IrO_3 under high pressure, *Physical Review B* **105**, 144402 (2022).
- [21] S. Pal, P. Malavi, A. Sinha, A. Ali, P. Sakrikar, B. Joseph, U. V. Waghmare, Y. Singh, D. V. S. Muthu, S. Karmakar, and A. K. Sood, Pressure tuning of structure, magnetic frustration, and carrier conduction in the Kitaev spin liquid candidate Cu_2IrO_3 , *Physical Review B* **107**, 085105 (2023).
- [22] L. S. I. Veiga, M. Etter, K. Glazyrin, F. Sun, C. A. Eschelhoela, G. Fabbris, J. R. L. Mardegan, P. S. Malavi, Y. Deng, P. P. Stavropoulos, H. Y. Kee, W. G. Yang, M. Van Veenendaal, J. S. Schilling, T. Takayama, H. Takagi, and D. Haskel, Pressure tuning of bond-directional exchange interactions and magnetic frustration in the hyperhoneycomb iridate $\beta\text{-Li}_2\text{IrO}_3$, *Physical Review B* **96**, 140402(R) (2017).
- [23] L. S. I. Veiga, K. Glazyrin, G. Fabbris, C. D. Dashwood, J. G. Vale, H. Park, M. Etter, T. Irifune, S. Pascarelli, D. F. McMorrow, T. Takayama, H. Takagi, and D. Haskel, Pressure-induced structural dimerization in the hyperhoneycomb iridate $\beta\text{-Li}_2\text{IrO}_3$ at low temperatures, *Physical Review B* **100**, 064104 (2019).
- [24] V. Hermann, M. Altmeyer, J. Ebad-Allah, F. Freund, A. Jesche, A. A. Tsirlin, M. Hanfland, P. Gegenwart, I. I. Mazin, D. I. Khomskii, R. Valentí, and C. A. Kuntscher, Competition between spin-orbit coupling, magnetism, and dimerization in the honeycomb iridates: $\alpha\text{-Li}_2\text{IrO}_3$ under pressure, *Physical Review B* **97**, 020104(R) (2018).
- [25] J. P. Clancy, H. Gretarsson, J. A. Sears, Y. Singh, S. Desgreniers, K. Mehlawat, S. Layek, G. K. Rozenberg, Y. Ding, M. H. Upton, D. Casa, N. Chen, J. Im, Y. Lee, R. Yadav, L. Hozoi, D. Efremov, J. van den Brink, and Y.-J. Kim, Pressure-driven collapse of the relativistic electronic ground state in a honeycomb iridate, *npj Quantum Materials* **3**, 35 (2018).
- [26] C. Jin, J. Han, Q. Zheng, E. Chen, T. Pei, Y. Nakamoto, K. Shimizu, Y. Wang, and J. Zhu, Pressure-induced dimerization and crossover from negative to positive magnetoresistance in $\text{Ag}_3\text{LiIr}_2\text{O}_6$, *Physical Review B* **109**, 094411 (2024).
- [27] T. Takayama, A. Krajewska, A. S. Gibbs, A. N. Yaresko, H. Ishii, H. Yamaoka, K. Ishii, N. Hiraoka, N. P. Funnell, C. L. Bull, and H. Takagi, Pressure-induced collapse of the spin-orbital Mott state in the hyperhoneycomb iridate $\beta\text{-Li}_2\text{IrO}_3$, *Physical Review B* **99**, 125127 (2019).
- [28] See Supplemental Material at [url] for further details on the experimental setups, additional electrical transport, RIXS, and thermodynamic-path-dependent powder diffraction data, details on the analysis of XANES data, and Cu K edge XMCD data, which includes Refs. [12, 15, 19, 20, 25, 27, 29, 30, 32, 35, 51–64].
- [29] B. T. Thole and G. van der Laan, Linear relation between x-ray absorption branching ratio and valence-band spin-orbit expectation value, *Physical Review A* **38**, 1943 (1988).
- [30] P. Carra, B. T. Thole, M. Altarelli, and X. Wang, X-ray circular dichroism and local magnetic fields, *Physical Review Letters* **70**, 694 (1993).
- [31] The spin sum rule depends on the magnetic dipole operator $\langle T_z \rangle$ [30]. We use $\langle T_z \rangle / \langle S_z \rangle = 0.18$ obtained from theoretical calculations of Sr_2IrO_4 [34].
- [32] J. P. Clancy, N. Chen, C. Y. Kim, W. F. Chen, K. W. Plumb, B. C. Jeon, T. W. Noh, and Y.-J. Kim, Spin-orbit coupling in iridium-based 5d compounds probed by x-ray absorption spectroscopy, *Physical Review B* **86**, 195131 (2012).
- [33] M. A. Laguna-Marco, D. Haskel, N. Souza-Neto, J. C. Lang, V. V. Krishnamurthy, S. Chikara, G. Cao, and M. van Veenendaal, Orbital Magnetism and Spin-Orbit Effects in the Electronic Structure of BaIrO_3 , *Physical Review Letters* **105**, 216407 (2010).
- [34] D. Haskel, G. Fabbris, M. Zhernenkov, P. P. Kong, C. Q. Jin, G. Cao, and M. van Veenendaal, Pressure Tuning of the Spin-Orbit Coupled Ground State in Sr_2IrO_4 , *Physical Review Letters* **109**, 027204 (2012).
- [35] M. A. Laguna-Marco, P. Kayser, J. A. Alonso, M. J. Martínez-Lope, M. van Veenendaal, Y. Choi, and D. Haskel, Electronic structure, local magnetism, and spin-orbit effects of Ir(IV)-, Ir(V)-, and Ir(VI)-based compounds, *Physical Review B* **91**, 214433 (2015).
- [36] H. Gretarsson, J. P. Clancy, X. Liu, J. P. Hill, E. Bozin, Y. Singh, S. Manni, P. Gegenwart, J. Kim, A. H. Said, D. Casa, T. Gog, M. H. Upton, H.-S. Kim, J. Yu, V. M. Katukuri, L. Hozoi, J. van den Brink, and Y.-J. Kim, Crystal-Field Splitting and Correlation Effect on the Electronic Structure of A_2IrO_3 , *Physical Review Letters* **110**, 076402 (2013).
- [37] A. de la Torre, B. Zager, F. Bahrami, M. H. Upton, Y. Kim, G. Fabbris, G. H. Lee, W. Yang, D. Haskel, F. Tafti, and K. W. Plumb, Momentum-independent magnetic excitation continuum in the honeycomb iridate $\text{H}_3\text{LiIr}_2\text{O}_6$, *Nature Communications* **14**, 5018 (2023).
- [38] M. van Veenendaal and D. Haskel, Interpretation of ir L -edge isotropic x-ray absorption spectra across the pressure-induced dimerization transition in hyperhoneycomb $\beta\text{-Li}_2\text{IrO}_3$, *Physical Review B* **105**, 214420 (2022).
- [39] I. I. Mazin, H. O. Jeschke, K. Foyevtsova, R. Valentí, and D. I. Khomskii, Na_2IrO_3 as a Molecular Orbital Crystal, *Physical Review Letters* **109**, 197201 (2012).
- [40] A. Revelli, M. Moretti Sala, G. Monaco, P. Becker, L. Bohaty, M. Hermanns, T. C. Koethe, T. Frohlich, P. Warzanowski, T. Lorenz, S. V. Streltsov, P. H. M. van Loosdrecht, D. I. Khomskii, J. van den Brink, and M. Gruninger, Resonant inelastic x-ray incarnation of young's double-slit experiment, *Science Advances* **5**, eaav4020 (2019).
- [41] Y. Wang, R. Wang, J. Kim, M. H. Upton, D. Casa, T. Gog, G. Cao, G. Kotliar, M. P. M. Dean, and X. Liu, Direct detection of dimer orbitals in $\text{Ba}_5\text{Allr}_2\text{O}_{11}$, *Physical Review Letters* **122**, 106401 (2019).
- [42] A. P. Mackenzie, The properties of ultrapure delafossite metals, *Reports on Progress on Physics* **80**, 032501 (2017).

- [43] W. M. Xu, G. R. Hearne, and M. P. Pasternak, CuFeO_2 at a megabar: Stabilization of a mixed-valence low-spin magnetic semiconducting ground state, *Physical Review B* **94**, 035155 (2016).
- [44] W. M. Xu, G. K. Rozenberg, M. P. Pasternak, M. Kertzer, A. Kurnosov, L. S. Dubrovinsky, S. Pascarelli, M. Munoz, M. Vaccari, M. Hanfland, and R. Jeanloz, Pressure-induced $\text{Fe} \leftrightarrow \text{Cu}$ cationic valence exchange and its structural consequences: High-pressure studies of delafossite CuFeO_2 , *Physical Review B* **81**, 104110 (2010).
- [45] A. Garg and R. Rao, Copper delafossites under high pressure — a brief review of xrd and raman spectroscopic studies, *Crystals* **8**, 255 (2018).
- [46] D. Levy, E. Greenberg, S. Layek, M. P. Pasternak, I. Kantor, S. Pascarelli, C. Marini, Z. Konopkova, and G. K. Rozenberg, High-pressure structural and electronic properties of CuMO_2 ($M = \text{Cr}, \text{Mn}$) delafossite-type oxides, *Physical Review B* **101**, 245121 (2020).
- [47] K. V. Lawler, D. Smith, S. R. Evans, A. M. Dos Santos, J. J. Molaison, J. G. Bos, H. Mutka, P. F. Henry, D. N. Argyriou, A. Salamat, and S. A. J. Kimber, Decoupling lattice and magnetic instabilities in frustrated CuMnO_2 , *Inorganic Chemistry* **60**, 6004 (2021).
- [48] Y. Haraguchi, D. Nishio-Hamane, A. Matsuo, K. Kindo, and H. A. Katori, High-temperature magnetic anomaly via suppression of antisite disorder through synthesis route modification in a kitaev candidate Cu_2IrO_3 , *Journal of Physics: Condensed Matter* **36**, 405801 (2024).
- [49] M. Abramchuk, O. I. Lebedev, O. Hellman, F. Bahrami, N. E. Mordvinova, J. W. Krizan, K. R. Metz, D. Broido, and F. Tafti, Crystal chemistry and phonon heat capacity in quaternary honeycomb delafossites: $\text{Cu}[\text{Li}_{1/3}\text{Sn}_{2/3}]\text{O}_2$ and $\text{Cu}[\text{Na}_{1/3}\text{Sn}_{2/3}]\text{O}_2$, *Inorganic Chemistry* **57**, 12709 (2018).
- [50] M. Fisch, A. Lanza, E. Boldyreva, P. Macchi, and N. Casati, Kinetic control of high-pressure solid-state phase transitions: A case study on l-serine, *The Journal of Physical Chemistry C* **119**, 18611 (2015).
- [51] D. Haskel, Y. C. Tseng, N. M. Souza-Neto, J. C. Lang, S. Sinogeikin, Y. Mudryk, K. A. Gschneidner, and V. K. Pecharsky, Magnetic spectroscopy at high pressures using X-ray magnetic circular dichroism, *High Pressure Research* **28**, 185 (2008).
- [52] A. Dewaele, M. Torrent, P. Loubeyre, and M. Mezouar, Compression curves of transition metals in the Mbar range: Experiments and projector augmented-wave calculations, *Physical Review B* **78**, 104102 (2008).
- [53] M. Rivers, V. Prakapenka, A. Kubo, C. Pullins, C. Holl, and S. Jacobsen, The COMPRES/GSECARS gas-loading system for diamond anvil cells at the Advanced Photon Source, *High Pressure Research* **28**, 273 (2008).
- [54] M. Newville, Larch: An Analysis Package for XAFS and Related Spectroscopies, *Journal of Physics: Conference Series* **430**, 012007 (2013).
- [55] J. Kim, Advances in high-resolution RIXS for the study of excitation spectra under high pressure, *High Pressure Research* **36**, 391 (2016).
- [56] A. D. Chijioke, W. J. Nellis, A. Soldatov, and I. F. Silvera, The ruby pressure standard to 150 GPa, *Journal of Applied Physics* **98**, 114905 (2005).
- [57] S. T. Weir, J. Akella, C. Aracne-Ruddle, Y. K. Vohra, and S. A. Catledge, Epitaxial diamond encapsulation of metal microprobes for high pressure experiments, *Applied Physics Letters* **77**, 3400 (2000).
- [58] J. Lim, A. C. Hire, Y. Quan, J. Kim, L. Fanfarillo, S. R. Xie, R. S. Kumar, C. Park, R. J. Hemley, Y. K. Vohra, R. G. Hennig, P. J. Hirschfeld, G. R. Stewart, and J. J. Hamlin, High-pressure study of the low-Z rich superconductor Be_{22}Re , *Physical Review B* **104**, 064505 (2021).
- [59] W. B. Holzapfel, M. Hartwig, and W. Sievers, Equations of state for Cu, Ag, and Au for wide ranges in temperature and pressure up to 500 GPa and above, *Journal of Physical and Chemical Reference Data* **30**, 515 (2001).
- [60] D. D. Ragan, R. Gustavsen, and D. Schiferl, Calibration of the ruby R_1 and R_2 fluorescence shifts as a function of temperature from 0 to 600 K, *Journal of Applied Physics* **72**, 5539 (1992).
- [61] C. Prescher and V. B. Prakapenka, DIOPTAS : a program for reduction of two-dimensional X-ray diffraction data and data exploration, *High Pressure Research* **35**, 223 (2015).
- [62] G. van der Laan and A. I. Figueroa, X-ray magnetic circular dichroism—a versatile tool to study magnetism, *Coordination Chemistry Reviews* **277-278**, 95 (2014).
- [63] S. Nagamatsu, H. Matsumoto, T. Fujikawa, K. Ishiji, and H. Hashizume, Measurement and multiple-scattering calculation of cu K -edge x-ray magnetic circular dichroism spectra from an exchange-coupled Co/Cu multilayer, *Physical Review B* **70**, 174442 (2004).
- [64] A. A. Ivanov, V. G. Ivanov, A. P. Menushenkov, F. Wilhelm, A. Rogalev, A. Puri, B. Joseph, W. Xu, A. Marcelli, and A. Bianconi, Local noncentrosymmetric structure of $\text{Bi}_2\text{Sr}_2\text{CaCu}_2\text{O}_{8+y}$ by x-ray magnetic circular dichroism at Cu K -edge XANES, *Journal of Superconductivity and Novel Magnetism* **31**, 663 (2018).